NANO LETTERS

pubs.acs.org/NanoLett Letter

From Low-Field Sondheimer Oscillations to High-Field Very Large and Linear Magnetoresistance in a $SrTiO_3$-Based Two-Dimensional Electron Gas

Srijani Mallik, Gerbold C. Ménard, Guilhem Saïz, Ildar Gilmutdinov, David Vignolles, Cyril Proust, Alexandre Gloter, Nicolas Bergeal, Marc Gabay, and Manuel Bibes*

Cite This: *Nano Lett.* 2022, 22, 65−72 Read Online

ACCESS | Metrics & More | Article Recommendations | Supporting Information

ABSTRACT: Quantum materials harbor a cornucopia of exotic transport phenomena challenging our understanding of condensed matter. Among these, a giant, nonsaturating linear magnetoresistance (MR) has been reported in various systems, from Weyl semimetals to topological insulators. Its origin is often ascribed to unusual band structure effects, but it may also be caused by extrinsic sample disorder. Here, we report a very large linear MR in a $SrTiO_3$ two-dimensional electron gas and, by combining transport measurements with electron spectromicroscopy, show that it is caused by nanoscale inhomogeneities that are self-organized during sample growth. Our data also reveal semiclassical Sondheimer oscillations arising from interferences between helicoidal electron trajectories, from which we determine the 2DEG thickness. Our results bring insight into the origin of linear MR in quantum materials, expand the range of functionalities of oxide 2DEGs, and suggest exciting routes to explore the interaction of linear MR with features like Rashba spin−orbit coupling.

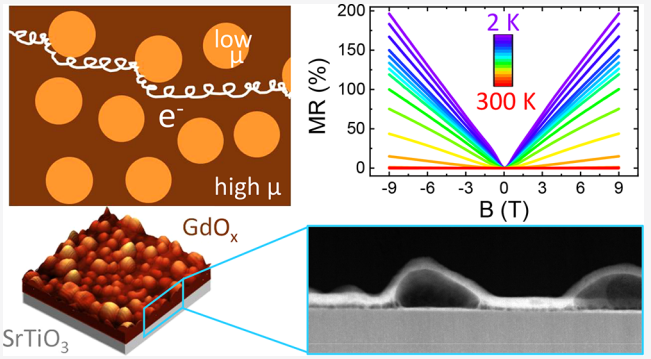

KEYWORDS: *2D electron gas, linear magnetoresistance, Sondheimer oscillations, oxide interfaces*

Since their discovery in 2004,[1] oxide two-dimensional electron gases (2DEGs) have been shown to possess a wide range of functionalities including superconductivity[2] and Rashba spin−orbit coupling (SOC).[3] Consequently, these 2DEGs display a rich phenomenology of electron transport. They commonly show Lorentz magnetoresistance, weak localization, and weak antilocalization due to the Rashba SOC.[3] Further, samples with high mobilities exhibit Shubnikov−de Haas oscillations[4,5] and the quantum Hall effect.[6] A peculiar angular dependence of the resistance, including a unidirectional magnetoresistance[7,8] and high order oscillations,[9] has also been reported.[8,10−12]

A few studies also mention a linear magnetoresistance (MR) for perpendicular magnetic field B [13,14] with, in some cases, a very large amplitude (>500% at 9 T).[13] This is reminiscent of a giant, nonsaturating linear MR reported in various systems including narrow band gap semiconductors,[15] graphene,[16,17] semimetals,[18−20] and topological insulators.[21,22] Two main scenarios have been proposed to explain this behavior. Abrikosov[23,24] established that impurity scattering of Dirac fermions confined to the lowest Landau level, modeling quasi-gapless semiconductors, results in a positive quantum MR varying linearly with B. Alternatively, Parish and Littlewood[25,26] introduced a classical model describing the behavior of charges moving through an array of four-terminal random resistors where they are subjected to a driving current along one direction and a magnetic field perpendicular to the array. These resistors represent regions where the mobility of the carriers fluctuate. The Lorentz force deflects the carrier trajectories, leading to Hall resistance in the local impedance matrix proportional to B. In the thermodynamic limit, when the width of the mobility distribution is less than the average, the network's impedance exhibits a positive MR that is linear in B and proportional to the average mobility above a crossover field B_C scaling with the inverse of the average mobility. Elaborating on this scenario, Kozlova et al.[27] considered the dynamics of high mobility two-dimensional classical electrons experiencing an in-plane longitudinal electric field and an out-of-plane magnetic field that are scattered off randomly placed, low mobility, large size islands. Multiple collisions on each island at the Hall velocity allow electrons to move around the obstacle and continue their course in the direction of the

Received: August 18, 2021
Revised: December 7, 2021
Published: December 16, 2021

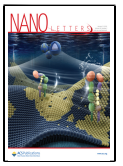

https://doi.org/10.1021/acs.nanolett.1c03198
Nano Lett. 2022, 22, 65−72

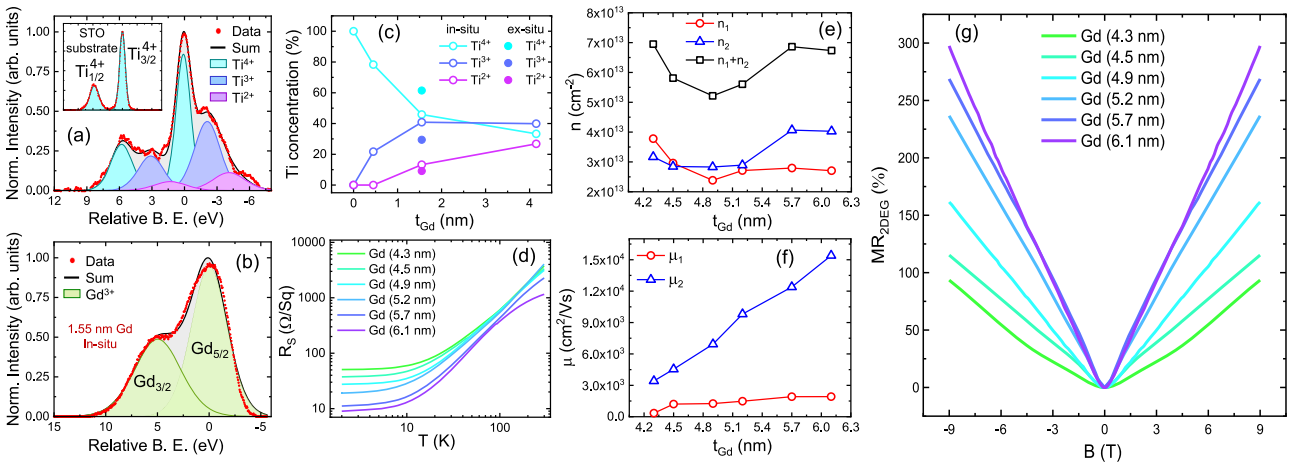

Figure 1. (a) X-ray photoelectron spectra (XPS) near the Ti 2p edge for a bare $SrTiO_3$ single crystal substrate (inset) and after deposition of 1.55 nm of Gd. The fitted peaks for Ti^{4+}, Ti^{3+}, Ti^{2+} and the sum fit envelope are shown in cyan, light blue, magenta colors, and solid black line, respectively. Two Ti peaks of same color correspond to the 3/2 (right) and 1/2 (left) splitting of that specific Ti valence state. (b) XPS spectra near Gd 3d edge after deposition of 1.55 nm of Gd. The fitted peaks with only Gd^{3+} states suggest the oxidation of the whole Gd layer. (c) Concentration of different Ti reduced states as a function of deposited Gd thickness. The hollow and the solid circles represent the state of the sample before and after exposure to the air, respectively. (d) Temperature dependence of the sheet resistance of GdO_x/STO samples of different thicknesses. (e, f) Carrier densities and the mobilities of the same samples extracted by fitting the Hall measurements and zero field sheet resistance at 2 K with two band model. (g) Magnetoresistance measurements of 2D electron gas (2DEG) present in the GdO_x/STO samples. The contribution of the 2DEG has been extracted by subtracting the metal contribution (if any) of Gd in the samples.

electric field. But this process causes an increase in the resistance that depends linearly on B above the crossover field. It dominates the magnetotransport response of the system at high field.

In this manuscript, we report a very large linear MR in $SrTiO_3$ (STO) 2DEGs generated by sputtering an ultrathin film of Gd onto (001)-oriented STO crystals. We investigate the temperature and gate dependence of the slope of the MR and the crossover field B_C and find that they scale with the mobility as expected from the Parish−Littlewood model. Unlike in most previous reports of giant linear MR interpreted within this scenario, we provide a direct characterization of the nanoscale disorder responsible for the effect through various microscopy techniques and electron energy-loss spectroscopy. In addition, we report the observation of oscillations in the resistance and its field derivatives that are periodic in B. We argue that they correspond to Sondheimer oscillations[28] and use them to extract a 2DEG thickness that agrees with the spectromicroscopy data.

We have deposited Gd films of various thicknesses by sputtering on STO (001) substrates. Prior to Gd deposition, the Ti valence of the STO substrates was studied *in situ* using X-ray photoelectron spectroscopy (XPS). The inset of Figure 1a shows the spectrum collected for the Ti 2p core levels of the substrate. Adventitious carbon was used as a charge reference to obtain the Ti^{4+} $2p_{3/2}$ peak position ~458.6 eV for the fitting. The energy difference between $2p_{3/2}$ and $2p_{1/2}$ was constrained to 5.7 eV. These values are consistent with values reported previously for STO.[29−31] We observed the sole presence of Ti^{4+} states indicative of stoichiometric STO, as expected. Further, Ti 2p core level spectra were measured *in situ* after depositing Gd. Figure 1a reveals additional peaks corresponding to Ti^{3+} and Ti^{2+} states reflecting the population of the Ti t_{2g} levels and the formation of the 2DEG. The relative concentration of Ti^{3+} and Ti^{2+} increases upon increasing Gd thickness t_{Gd} (Figure 1c), consistent with the situation observed in Y/STO heterostructures.[32] The study for Gd 3d core levels (Figure 1b) reveals that a 1.55 nm Gd film gets fully oxidized into Gd_2O_3. Therefore, it is clear that Gd reacts with the surface oxygen atoms of the STO substrate and gets fully oxidized by the creation of oxygen vacancies into STO. In a previous report[32] we showed that the degree of oxidation of various metals grown onto STO depends on their oxygen formation enthalpy and work function.[30,33] Here, we see that, owing to its much lower work function and more negative oxygen formation enthalpy in comparison to other metals (e.g., Al, Ta, Y), Gd induces a higher concentration of oxygen vacancies in STO. The solid circles in Figure 1c show the Ti concentration measured after exposing the sample to the air. Clearly, the amount of Ti^{3+} and Ti^{2+} decreases due to the reoxidation of the 2DEG, consistent with results from ref 32. Therefore, we deduced the critical thickness of Gd to avoid the reoxidation of the reduced Ti from the air and thus for all the samples studied t_{Gd} > 4 nm.

To confirm the generation of a 2DEG at the Gd/STO interface, we measured the temperature dependence of the sheet resistance R_S for samples having various Gd thicknesses (Figure 1d). A metallic behavior is observed for all samples. R_S drops by almost 2 orders of magnitude from 300 to 2 K, which validates the formation of 2DEG as inferred from XPS. At 2 K R_S decreases monotonically upon increasing t_{Gd}. At 2 K the Hall traces for these samples were nonlinear (Figure S1a, Supporting Information) suggesting that transport proceeds in a multiband regime. We extracted the carrier densities (n_1 and n_2) and mobilities (μ_1 and μ_2) of the 2DEGs by fitting the Hall data and the sheet resistance with a 2-band model,[34] cf. Figure 1e and Figure 1f. While the carrier densities do not change much with t_{Gd}, the mobilities increase dramatically. Typical mobilities of metal/STO 2DEGs are within the range of 1000 $cm^2/(V\ s)$ [32] but reach values as high as 15 000 $cm^2/(V\ s)$ for t_{Gd} = 6.1 nm. A crossover in the carrier densities for low and high mobility carriers is observed at t_{Gd} = 4.5 nm. Such a crossover is explained later in this paper with respect to carrier overdoping. Assuming parabolic dispersion, we extract for the

https://doi.org/10.1021/acs.nanolett.1c03198
Nano Lett. 2022, 22, 65−72

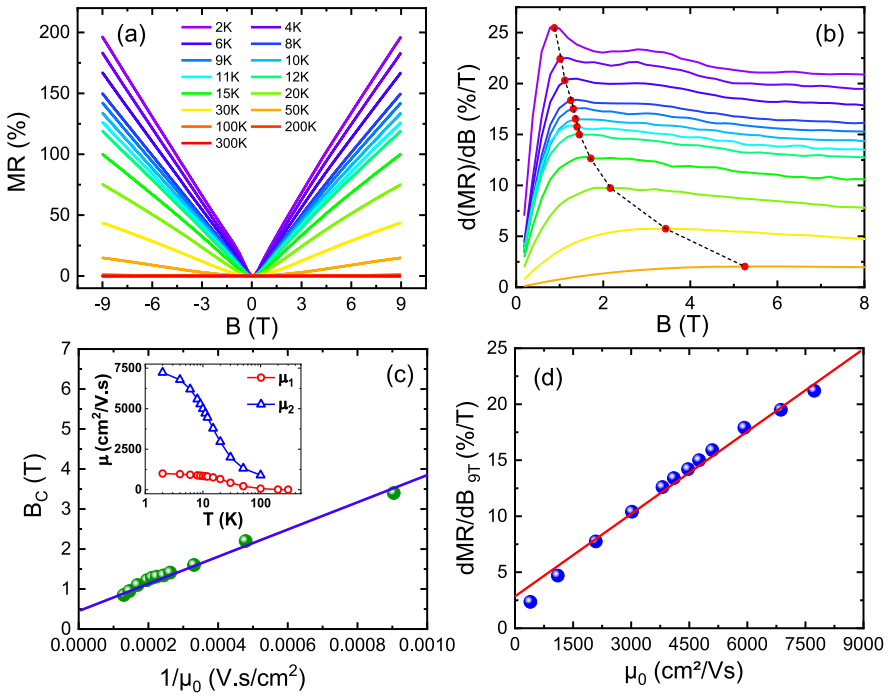

Figure 2. (a) Temperature dependent magnetoresistance curves for GdO_x (6.1 nm)/STO sample. (b) First derivative of the magnetoresistance curves (shown in (a)) with respect to the magnetic field. The crossover field (B_C) where the transition occurs from Lorentz MR to linear MR is indicated by the red solid circles on each curve. The color scheme for the temperatures is the same as in (a). (c) Crossover field vs inverse of the zero field mobility measured at various temperatures. Inset: temperature dependent mobilities extracted from the fits of the Hall measurements using the two band model. (d) First derivative of MR at 9 T as a function of zero field mobilities for different measurement temperatures. The blue and red straight lines connecting all the data points in (c) and (d), respectively, suggest that scattering phenomena for all the temperatures are dominated by a single mechanism.

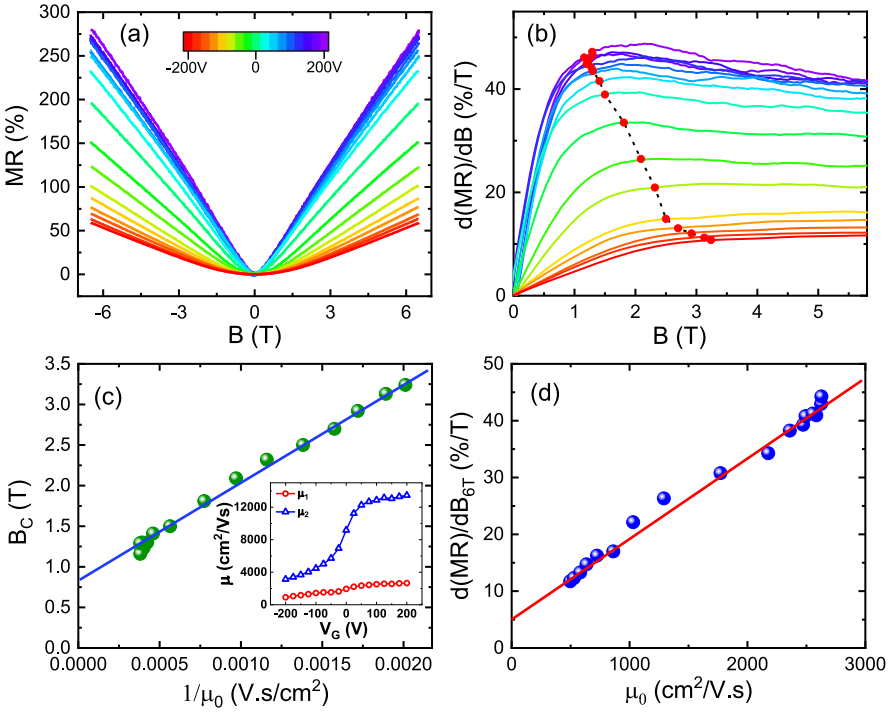

Figure 3. (a) Gate voltage dependent magnetoresistance curves for GdO_x (6.1 nm)/STO sample at T = 2 K. (b) First derivative of the magnetoresistance curves (shown in (a)) with respect to the magnetic field. The crossover field (B_C) corresponds to the red solid circle on each curve. The color scheme for the gate voltages is the same as in (a). (c) Crossover field vs inverse of the zero field mobility for different gate voltages. Inset: gate voltage dependent mobilities extracted from the fittings of the Hall measurements using the two band model. (d) First derivative of MR at 6 T as a function of the zero field mobilities for different gate voltages. The blue and red straight lines connecting all the data points in (c) and (d), respectively, suggest that scattering phenomena for all the gate voltages are dominated by a single mechanism.

https://doi.org/10.1021/acs.nanolett.1c03198
Nano Lett. 2022, 22, 65−72

6.1 nm sample a mean free path $l_1 = 0.13\ \mu$m (respectively $l_2 = 1.6\ \mu$m) for the low (respectively high) mobility carriers. Since l_1 and l_2 are quite large, we expect a semiclassical kinetic description of transport, allowing us to use the scaling established in refs 25 and 27. The MR curves at 2 K are shown in Figure 1g. The large MR (in the 200% range) displays an unusual linear behavior and does not appear to saturate with B. All samples display a crossover (B_C) between a low-field parabolic MR and a high-field linear MR (particularly clear for the 4.3 nm sample). Both the MR value and the dominance of the linear behavior increase with t_{Gd}.

Figure 2a depicts the temperature dependent MR data for a 6.1 nm sample. The MR decreases upon increasing temperature, but its linear nature persists up to at least 50 K. This suggests that the MR has a classical origin as the effect is not observed at low temperature only. Due to the high oxidation affinity of Gd, the samples show an aging effect that is reflected by the decrease in MR from ∼300% to ∼200% for $t_{Gd} = 6.1$ nm sample as observed from Figures 1g and 2a. A crossover between parabolic and linear behavior is again clearly visible. Figure 2b shows the first derivative of the temperature dependent MR curves where B_C values are pointed by red solid circles. The position of the crossover fields is determined by the first maxima of the first derivatives of the MR curves. The low temperature data also reveal oscillations that we will discuss later. We have also measured the Hall effect at various temperatures (Figure S2 in Supporting Information) and extracted the carrier densities and mobilities (cf. inset of Figure 2c). To test the applicability of the Parish−Littlewood model to our samples, we plot the dependence of the crossover field with the inverse of the zero field mobility (μ_0) in Figure 2c: as expected, a linear dependence is obtained. The zero field mobilities are calculated using the formula $\mu_0 = 1/(enR_S(B=0))$ where n is the carrier density obtained from the Hall data and $R_S(B=0)$ is the sheet resistance at $B = 0$ T. Figure 2d shows that the slope of the linear MR scales with μ_0, also consistent with the Parish and Littlewood model. Interestingly, these data provide an estimate of the fraction f of low-mobility islands in the sample. The slope of the MR in the linear regime is given by $\frac{\mathrm{d\,MR}}{\mathrm{d}B} \sim \mu^* B$,[27] where the effective mobility is $\mu^* = \mu_0\left(\frac{f}{2(1-f)}\right)$. From Figure 2b, we get $\frac{\mathrm{d\,MR}}{\mathrm{d}B} \sim 0.22$/T and we determine $\mu_0 \sim 0.62$ m^2/(V s) at 2 K. Accordingly, we find $f \sim 0.4$.

Figure 3a shows the back gate voltage (V_G) dependence of magnetoresistance at $T = 2$ K. For $V_G > -75$ V the linear MR dominates over the parabolic MR. However, for -75 V $> V_G > -200$ V the parabolic MR becomes more prominent. As for the data of Figure 2, the crossover field values were calculated from the first derivative of the MR curves (Figure 3b). The carrier densities and the mobilities were also calculated using a similar two band model. A crossover in the carrier density plot (Figure S3b in Supporting Information) is observed while decreasing the gate voltage from 200 V to −200 V. For the depleted region ($V_G < 0$ V) the sample behaves as usual LAO/STO 2DEGs with minority carrier having a higher mobility. However, in the overdoped regime ($V_G > 0$ V), a crossover occurs and the high mobility carriers become dominant. The inset of Figure 3c shows the gate dependence of the mobilities, revealing a sharp transition/increase around $V_G = -75$ V. This probably signifies a transition between a set of light and/or heavy bands coexisting throughout the explored doping range. Consistent with the temperature dependent data, the crossover field scales linearly with the inverse of the zero field mobility (Figure 3c). Further, the value of the first derivative of the MR at 6 T scales linearly with the zero field mobilities for the respective gate voltages (Figure 3d). This confirms the classical origin of the linear MR behavior in our system and supports our interpretation in the framework of the Parish−Littlewood model.

We now discuss the oscillations observed in the derivative of the MR displayed in Figure 2b. When a magnetic field is applied perpendicular to the applied current, electrons perform cyclotron motion, leading to the quantization of the Fermi surface through the appearance of Landau levels. In this regime the resistance displays maxima and minima as the magnetic field is varied, called Shubnikov−de Haas (SdH) oscillations that appear at high field with a period scaling with $1/B$. In Figure 4b we plot the second derivative of the MR in which the

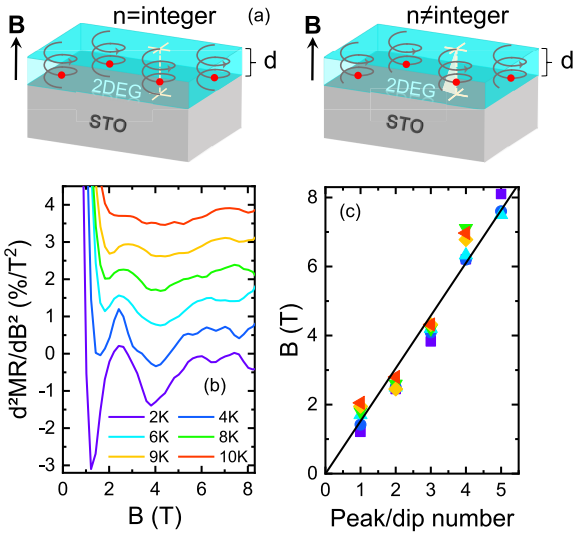

Figure 4. (a) Schematic representation of the mechanism of Sondheimer oscillations in STO 2DEGs. d and B represent the thickness of the 2DEG and the applied magnetic field, respectively. The red solid circles are the electrons, and their helical motion in the magnetic field in the z-direction is represented as gray lines. If the number of revolutions (n) needed for an electron to go from the top surface to the bottom is an integer, then no net motion of the electron should be seen in the x−y plane (left). On the contrary, if n becomes a noninteger, then a net motion of the electron is seen in the x−y plane (right). (b) Sondheimer oscillations from second derivative of the magnetoresistance curves for $T = 2$ to 10 K. (c) Peak and dip number with respect to their positions, i.e., corresponding magnetic field values.

oscillations are more visible. They are present at low field, and their period roughly scales with B (cf. Figure 4c). Thus, they cannot be SdH oscillations. When undergoing cyclotron motion in the plane perpendicular to magnetic field, electrons may also acquire a net velocity in the magnetic field direction. The electrons then follow helical trajectories, which, as described by Sondheimer,[28] may also produce resistance oscillations. Figure 4a depicts the schematic representation of Sondheimer oscillations in a conductive slab. For a given slab thickness and perpendicular electron velocity, the radius of the helical path and the number of revolutions (n) to travel from one surface to the other are determined by the applied magnetic field. If n is an integer (top left Figure 4a) no relative

https://doi.org/10.1021/acs.nanolett.1c03198
Nano Lett. 2022, 22, 65−72

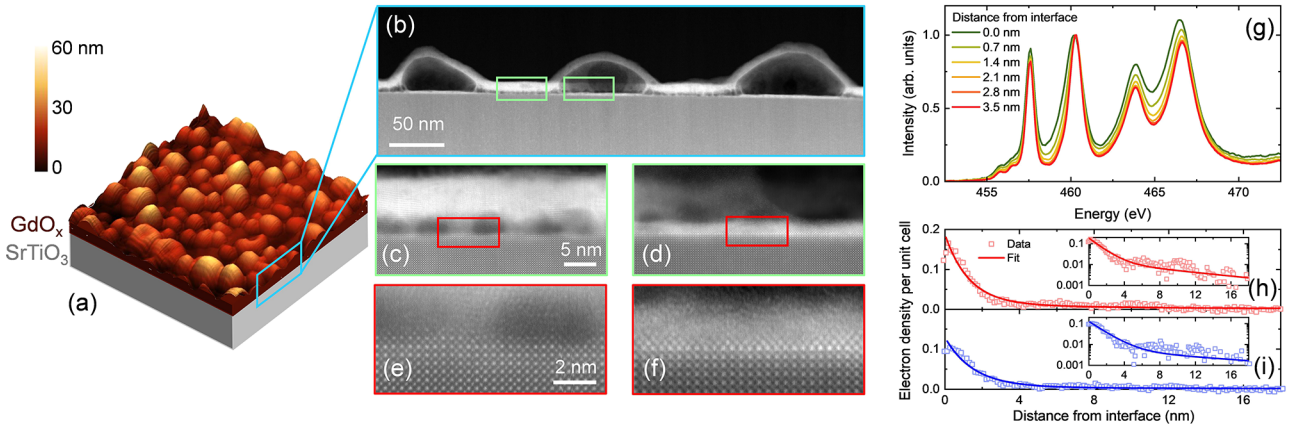

Figure 5. (a) 3D view of the topography of GdO_x/STO sample by atomic force microscopy exhibits bubbles of GdO_x due to oxidation. (b) Low magnification high-angle annular dark field (HAADF) scanning transmission electron microscopy (STEM) image at the cross section (marked by the blue box) of the GdO_x blisters. (c, d) HAADF images of the interface beside and below the bubble, respectively, as marked by the green boxes in (b). (e, f) Inset zoom on the last STO plane for beside and below the bubble, respectively, as marked by the red boxes in (c) and (d). (g) Electron energy loss spectroscopy (EELS) spectra showing typical Ti-L edges evolution over the 4 nm on top of the STO. (h, i) Charge profile as a function of the distance from the interface inside STO for below and beside the bubble, respectively. It shows a slightly sharper feature below the bubble in accordance with the sharper interface shown in (f). The insets are the zoom on the tail of the corresponding depth profiles.

motion of the electron is observed in the plane. However, when n is a noninteger (top right, Figure 4a) a net in-plane motion (displacement with respect to the initial position in-plane) occurs. This results in an oscillatory MR behavior. Interestingly, the thickness of the conductive slab (here the 2DEG) can be determined from the period of the oscillations. To do that, we consider the time needed for the carriers to undergo one cyclotron revolution that is $t_C = 2\pi/\omega_C = 2\pi m/(eB)$ (where ω_C, e, and m are the cyclotron frequency, electron charge, and electron mass, respectively) and the time needed to cross the 2DEG vertically is $t = d/v_z$ (where d is the thickness of the 2DEG and v_z is the velocity of electrons along the z direction). A Sondheimer oscillation occurs when $t = n \times t_C$ and thus $v_z = e\Delta B d/(2\pi m)$. The finite value of v_z is a consequence of the slight wobbling of the Fermi surface along k_z which occurs when several sub-bands are occupied.[35,36] Now, considering a cylindrical Fermi surface, $v_z = \hbar k_F^z/m_z = \hbar/(m_z d)$ where m_z is the effective mass of electrons along z. By equating v_z from both equations, $d = \sqrt{\frac{hm}{\Delta B e m_z}}$ where $\Delta B = 3$ T from Figure 4b and $m_z/m = 8$ from both the out-of-plane and in-plane magnetotransport data (Figure S5 in Supporting Information). This value is consistent with the $m_z/m \sim 11-15$ estimates of refs 35 and 36. Therefore, we determine the thickness of the 2DEG to be ~13 nm.

We finally return to the origin of the linear MR and to our interpretation within the Parish–Littlewood model assuming inhomogeneous transport. From our extraction of the mobilities and mean free paths, we estimate the average distance between the inhomogeneities to be of order $l_1 \approx 130$ nm. Let us now compare this number with values deduced from structural characterization.

As visible from the atomic force microscopy (AFM) image shown in Figure 5a, Gd/STO samples have a peculiar surface morphology. While LAO/STO or AlO_x/STO 2DEG samples are usually atomically smooth, here AFM reveals the presence of mesoscopic outgrowths with a height of around 30 nm and a diameter of 50–100 nm. We note that their average distance is comparable to the estimate mentioned above. Yet, the height and density of these outgrowths are particularly surprising given the thickness of the deposited Gd, here only 6.1 nm.

To gain insight into their nature, we have performed transmission electron microscopy. Figure 5b shows a cross section through three outgrowths. They appear to be hollow, having the same morphology as blisters, explaining the apparent inconsistency between their large height and the low deposited Gd thickness. Elemental analysis reveals the presence of a ~2.5 nm thick amorphous layer of GdO_x with some interdiffused Ti over the whole STO substrate and of a ~6 nm layer of crystalline GdO_x forming blisters. Below the blisters (Figure 5d), the amorphous layer is quite homogeneous and the STO/Ti:GdO_x interface is well-defined. Beside the blisters (Figure 5c), the amorphous layer is more discontinuous and the STO/Ti:GdO_x interface is rougher. The last STO planes beside and below the bubbles are zoomed in Figure 5e,f for better visibility. A possible mechanism leading to the formation of these mesostructures is the volume expansion and the stress modification of the Gd layer during its oxidation by the STO substrate.[37,38]

The chemical analysis reveals differences between the regions located below or beside the blisters, with sharper Gd and Ti profiles below the blisters. The EELS fine structure of the Ti $L_{3,2}$ edges (Figure 5g) indicates that the Ti valence is different from pure 4+, consistent with XPS. Fits of the EELS spectra with reference components allow extracting the fraction of Ti^{3+} (i.e., the electron density). The corresponding profiles below and beside the blisters are plotted in Figure 5h and Figure 5i, respectively. One first notices that the electron density is higher below the blisters than beside them, which suggests that below the blisters the mobility is lower,[39] thus clarifying the origin of the inhomogeneous transport. Analyzing the height distribution of the AFM image, we estimate that the outgrowths fill ~36% of the sample surface, which matches well the fraction of low-mobility regions extracted from the MR data (40%).

Both electron density profiles can be well fitted with the sum of two decaying exponentials, with characteristic decay lengths of 1.3 and 10 nm below the blisters and 1.5 and 14.3 nm beside the blisters. The shortest decay lengths match well the

https://doi.org/10.1021/acs.nanolett.1c03198
Nano Lett. 2022, 22, 65–72

estimates of the 2DEG thickness for LAO/STO,[29] where 2DEG formation is believed to mostly arise from interfacial charge transfer that may also be at play here. The longest decay lengths are indicators of the total 2DEG thickness and are consistent with the generation of carriers through the formation of oxygen vacancies in the STO, created by the deposition of Gd. Remarkably, these decay lengths are in good agreement with our estimate of the 2DEG thickness from the Sondheimer oscillations (~13 nm).

In summary, we have observed a very large linear magnetoresistance in STO 2DEGs induced by the formation of 50−100 nm wide blisters during the deposition of a nanometric Gd film. This peculiar magnetotransport response could be investigated in more detail and more systematically in high-quality, homogeneous STO or $KTaO_3$ 2DEG samples[44] patterned at the nanoscale to induce inhomogeneities with controlled dimensions and densities. In addition, we have identified the presence of Sondheimer oscillations, for the first time in oxide 2DEGs, and used their period to extract an accurate estimate of the 2DEG thickness. Sondheimer oscillations thus emerge as a new tool to investigate the physics of such systems, as has recently been done for other quantum materials.[40]

MATERIALS AND METHODS

Sample Preparation and XPS. Gd thin films were deposited at room temperature by dc magnetron sputtering on as received STO (001) substrates from CrysTec. During Gd deposition, the Ar partial pressure and the dc power were kept fixed at 5.2×10^{-4} mbar and 11 W, respectively. The deposition rate was ~1 Å/s. XPS was performed using a nonmonochromatized Mg Kα source at 20 mA and 15 kV. Spectral analysis was carried out using CasaXPS.

Magnetotransport. Magnetotransport measurements were performed using a PPMS Dynacool system. The samples were bonded with Al wire in van der Pauw and Hall geometry for the magnetoresistance and Hall measurements, respectively. At the lowest temperature, the gate voltage was first increased to its maximum value (+200 V) to suppress hysteresis and ensure the full reversibility of the measurements in the gate range [−200 V, +200 V].[41] The electron density and mobility of the two populations of electron were extracted by combining the Hall effect and gate capacitance measurements as a function of gate voltage.[42]

Structural Analysis. Surface topography was measured using atomic force microscopy. The average size of the Gd blisters and the area covered by these blisters were analyzed using Gwyddion. STEM was done using (monochromated) Cs-corrected Nion microscopes. The operating voltage was set to 100 keV in order to limit electron beam damage. EELS was collected with EMCCD detector and Merlin EM direct electron detector respectively mounted on a 3 and a 4/5 orders corrected EELS spectrometer. The EELS chemical analysis was done by analyzing the Gd-N, Ti-L, and Gd-M edges. The EELS valence quantification was done by fitting the Ti-L edges with reference spectra ($SrTiO_3$ substrate at ~30 nm from the interface and a reference $DyTiO_3$.[43]

ASSOCIATED CONTENT

Supporting Information

The Supporting Information is available free of charge at https://pubs.acs.org/doi/10.1021/acs.nanolett.1c03198.

Thickness, temperature, and gate voltage dependent Hall data and their fits as well as the gate voltage dependent high field magnetoresistance data and in-plane magnetoresistance data (PDF)

AUTHOR INFORMATION

Corresponding Author

Manuel Bibes − *Unité Mixte de Physique, CNRS, Thales, Université Paris-Saclay, 91767 Palaiseau, France;* orcid.org/0000-0002-6704-3422; Email: manuel.bibes@cnrs-thales.fr

Authors

Srijani Mallik − *Unité Mixte de Physique, CNRS, Thales, Université Paris-Saclay, 91767 Palaiseau, France*

Gerbold C. Ménard − *Laboratoire de Physique et d'Etude des Matériaux, ESPCI Paris, PSL University, CNRS, Sorbonne Université, 75005 Paris, France*

Guilhem Saïz − *Laboratoire de Physique et d'Etude des Matériaux, ESPCI Paris, PSL University, CNRS, Sorbonne Université, 75005 Paris, France*

Ildar Gilmutdinov − *LNCMI-EMFL, CNRS, Université Grenoble Alpes, INSA-T, UPS, 31400 Toulouse, France*

David Vignolles − *LNCMI-EMFL, CNRS, Université Grenoble Alpes, INSA-T, UPS, 31400 Toulouse, France*

Cyril Proust − *LNCMI-EMFL, CNRS, Université Grenoble Alpes, INSA-T, UPS, 31400 Toulouse, France*

Alexandre Gloter − *Laboratoire de Physique des Solides, Université Paris-Saclay, CNRS UMR 8502, 91405 Orsay, France*

Nicolas Bergeal − *Laboratoire de Physique et d'Etude des Matériaux, ESPCI Paris, PSL University, CNRS, Sorbonne Université, 75005 Paris, France*

Marc Gabay − *Laboratoire de Physique des Solides, Université Paris-Saclay, CNRS UMR 8502, 91405 Orsay, France*

Complete contact information is available at: https://pubs.acs.org/10.1021/acs.nanolett.1c03198

Notes

The authors declare no competing financial interest.

ACKNOWLEDGMENTS

The authors thank A. Vecchiola for collecting the AFM image, X. Li for helping with the STEM-EELS experiments and P. Noël for discussions at an early stage of this study. This project received funding from the ERC Advanced "FRESCO" Grant 833973, from the H2020-EU "ESTEEM3" Grant 823717 and from the ANR "QUANTOP" grant. The high field magnetoresistance measurements were performed at the LNCMI, a member of the European Magnetic Field Laboratory.

REFERENCES

(1) Ohtomo, A.; Hwang, H. Y.; Reyren, N. A high-mobility electron gas at the $LaAlO_3/SrTiO_3$ heterointerface. *Nature* **2004**, *427*, 423−426.

(2) Reyren, N.; Thiel, S.; Caviglia, A. D.; Kourkoutis, L. F.; Hammerl, G.; Richter, C.; Schneider, C. W.; Kopp, T.; Thiel, S.; Caviglia, A.D.; Fitting Kourkoutis, L.; Hammerl, G.; Richter, C.; Schneider, C.W.; Kopp, T.; Rüetschi, A.-S.; Jaccard, D.; Gabay, M.; Muller, D. A.; Triscone, J.-M.; Mannhart, J. Superconducting Interfaces Between Insulating Oxides. *Science* **2007**, *317*, 1196−1199.

(3) Caviglia, A. D.; Gabay, M.; Gariglio, S.; Reyren, N.; Cancellieri, C.; Triscone, J.-M. Tunable Rashba Spin-Orbit Interaction at Oxide Interfaces. *Phys. Rev. Lett.* **2010**, *104*, 126803.
(4) Ben Shalom, M.; Ron, A.; Palevski, A.; Dagan, Y. Shubnikov−De Haas Oscillations in $SrTiO_3/LaAlO_3$ Interface. *Phys. Rev. Lett.* **2010**, *105*, 206401.
(5) Fête, A.; Gariglio, S.; Berthod, C.; Li, D.; Stornaiuolo, D.; Gabay, M.; Triscone, J.-M. Large modulation of the Shubnikov−de Haas oscillations by the Rashba interaction at the $LaAlO_3/SrTiO_3$ interface. *New J. Phys.* **2014**, *16*, 112002.
(6) Trier, F.; Prawiroatmodjo, G. E.; Zhong, Z.; Christensen, D. V.; von Soosten, M.; Bhowmik, A.; Lastra, J. M. G.; Chen, Y.; Jespersen, T. S.; Pryds, N. Quantization of Hall Resistance at the Metallic Interface between an Oxide Insulator and $SrTiO_3$. *Phys. Rev. Lett.* **2016**, *117*, 096804.
(7) Choe, D.; Jin, M.-J.; Kim, S.-I.; Choi, H.-J.; Jo, J.; Oh, I.; Park, J.; Jin, H.; Koo, H. C.; Min, B.-C.; Hong, S.; Lee, H.-W.; Baek, S.-H.; Yoo, J.-W. Gate-tunable giant nonreciprocal charge transport in noncentrosymmetric oxide interfaces. *Nat. Commun.* **2019**, *10*, 4510.
(8) Vaz, D. C.; Trier, F.; Dyrdał, A.; Johansson, A.; Garcia, K.; Barthélémy, A.; Mertig, I.; Barnaś, J.; Fert, A.; Bibes, M. Determining the Rashba parameter from the bilinear magnetoresistance response in a two-dimensional electron gas. *Physical Review Materials* **2020**, *4*, 071001.
(9) Joshua, A.; Ruhman, J.; Pecker, S.; Altman, E.; Ilani, S. Gate-tunable polarized phase of two-dimensional electrons at the $LaAlO_3/SrTiO_3$ interface. *Proc. Natl. Acad. Sci. U. S. A.* **2013**, *110*, 9633.
(10) Trushin, M.; Výborný, K.; Moraczewski, P.; Kovalev, A. A.; Schliemann, J.; Jungwirth, T. Anisotropic magnetoresistance of spin-orbit coupled carriers scattered from polarized magnetic impurities. *Phys. Rev. B: Condens. Matter Mater. Phys.* **2009**, *80*, 134405.
(11) Bovenzi, N.; Diez, M. Semiclassical theory of anisotropic transport at $LaAlO_3SrTiO_3$ interfaces under an in-plane magnetic field. *Phys. Rev. B: Condens. Matter Mater. Phys.* **2017**, *95*, 205430.
(12) Fête, A.; Gariglio, S.; Caviglia, A. D.; Triscone, J.-M.; Gabay, M. Rashba induced magnetoconductance oscillations in the $LaAlO_3$-$SrTiO_3$ heterostructure. *Phys. Rev. B* **2012**, *86*, No. 201105(R).
(13) Jin, H.; Lee, K.; Baek, S.-H.; Kim, J.-S.; Cheong, B.-k.; Park, B. H.; Yoon, S.; Suh, B. J.; Kim, C.; Seo, S. S. A.; Lee, S. Large linear magnetoresistance in heavily-doped Nb:SrTiO3 epitaxial thin films. *Sci. Rep.* **2016**, *6*, 34295.
(14) Kormondy, K. J.; Gao, L.; Li, X.; Lu, S.; Posadas, A. B.; Shen, S.; Tsoi, M.; McCartney, M. R.; Smith, D. J.; Zhou, J.; Lev, L. L.; Husanu, M.-A.; Strocov, V. N.; Demkov, A. A. Large positive linear magnetoresistance in the two-dimensional t2g electron gas at the $EuO/SrTiO_3$ interface. *Sci. Rep.* **2018**, *8*, 7721.
(15) Hu, J.; Parish, M. M.; Rosenbaum, T. F. Nonsaturating magnetoresistance of inhomogeneous conductors: Comparison of experiment and simulation. *Phys. Rev. B: Condens. Matter Mater. Phys.* **2007**, *75*, 214203.
(16) Wang, W. J.; Gao, K. H.; Li, Z. Q.; Lin, T.; Li, J.; Yu, C.; Feng, Z. H. Classical linear magnetoresistance in epitaxial graphene on SiC. *Appl. Phys. Lett.* **2014**, *105*, 182102.
(17) Kisslinger, F.; Ott, C.; Heide, C.; Kampert, E.; Butz, B.; Spiecker, E.; Shallcross, S.; Weber, H. B. Linear magnetoresistance in mosaic-like bilayer graphene. *Nat. Phys.* **2015**, *11*, 650−653.
(18) Liang, T.; Gibson, Q.; Ali, M. N.; Liu, M.; Cava, R. J.; Ong, N. P. Ultrahigh mobility and giant magnetoresistance in the Dirac semimetal Cd_3As_2. *Nat. Mater.* **2015**, *14*, 280−284.
(19) Huang, X.; Zhao, L.; Long, Y.; Wang, P.; Chen, D.; Yang, Z.; Liang, H.; Xue, M.; Weng, H.; Fang, Z.; Dai, X.; Chen, G. Observation of the Chiral-Anomaly-Induced Negative Magnetoresistance in 3D Weyl Semimetal TaAs. *Phys. Rev. X* **2015**, *5*, 031023.
(20) Narayanan, A.; Watson, M. D.; Blake, S. F.; Bruyant, N.; Drigo, L.; Chen, Y. L.; Prabhakaran, D.; Yan, B.; Felser, C.; Kong, T.; Canfield, P. C.; Coldea, A. I. Linear Magnetoresistance Caused by Mobility Fluctuations in *n*-Doped Cd_3As_2. *Phys. Rev. Lett.* **2015**, *114*, 117201.
(21) Yan, Y.; Wang, L.-X.; Yu, D.-P.; Liao, Z.-M. Large magnetoresistance in high mobility topological insulator Bi2Se3. *Appl. Phys. Lett.* **2013**, *103*, 033106.
(22) Leng, P.; Chen, F.; Cao, X.; Wang, Y.; Huang, C.; Sun, X.; Yang, Y.; Zhou, J.; Xie, X.; Li, Z.; Zhang, E.; Ai, L.; Yang, Y.; Xiu, F. Gate-Tunable Surface States in Topological Insulator β-Ag_2Te with High Mobility. *Nano Lett.* **2020**, *20*, 7004−7010.
(23) Abrikosov, A. A. Quantum magnetoresistance. *Phys. Rev. B: Condens. Matter Mater. Phys.* **1998**, *58*, 2788−2794.
(24) Abrikosov, A. A. Quantum linear magnetoresistance; solution of an old mystery. *J. Phys. A: Math. Gen.* **2003**, *36*, 9119−9131.
(25) Parish, M. M.; Littlewood, P. B. Non-saturating magnetoresistance in heavily disordered semiconductors. *Nature* **2003**, *426*, 162−165.
(26) Parish, M. M.; Littlewood, P. B. Classical magnetotransport of inhomogeneous conductors. *Phys. Rev. B: Condens. Matter Mater. Phys.* **2005**, *72*, 094417.
(27) Kozlova, N.; Mori, N.; Makarovsky, O.; Eaves, L.; Zhuang, Q.; Krier, A.; Patanè, A. Linear magnetoresistance due to multiple-electron scattering by low-mobility islands in an inhomogeneous conductors. *Nat. Commun.* **2012**, *3*, 1097−1101.
(28) Sondheimer, E. H. The Influence of a Transverse Magnetic Field on the Conductivity of Thin Metallic Films. *Phys. Rev.* **1950**, *80*, 401−406.
(29) Sing, M.; Berner, G.; Goß, K.; Müller, A.; Ruff, A.; Wetscherek, A.; Thiel, S.; Mannhart, J.; Pauli, S. A.; Schneider, C. W.; Willmott, P. R.; Gorgoi, M.; Schäfers, F.; Claessen, R. Profiling the Interface Electron Gas of $LaAlO_3/SrTiO_3$ Heterostructures with Hard X-Ray Photoelectron Spectroscopy. *Phys. Rev. Lett.* **2009**, *102*, 176805.
(30) Vaz, D. C.; Lesne, E.; Sander, A.; Naganuma, H.; Jacquet, E.; Santamaria, J.; Barthélémy, A.; Bibes, M. Tuning Up or Down the Critical Thickness in $LaAlO_3/SrTiO_3$ through In Situ Deposition of Metal Overlayers. *Adv. Mater.* **2017**, *29*, 1700486.
(31) Vaz, D. C.; et al. Mapping spin−charge conversion to the band structure in a topological oxide two-dimensional electron gas. *Nat. Mater.* **2019**, *18*, 1187−1193.
(32) Vicente-Arche, L. M.; Mallik, S.; Cosset-Cheneau, M.; Noël, P.; Vaz, D. C.; Trier, F.; Gosavi, T. A.; Lin, C.-C.; Nikonov, D. E.; Young, I. A.; Sander, A.; Barthélémy, A.; Attané, J.-P.; Vila, L.; Bibes, M. Metal/ $SrTiO_3$ two-dimensional electron gases for spin-to-charge conversion. *Physical Review Materials* **2021**, *5*, 064005.
(33) Posadas, A. B.; Kormondy, K. J.; Guo, W.; Ponath, P.; Geler-Kremer, J.; Hadamek, T.; Demkov, A. A. Scavenging of oxygen from $SrTiO_3$ during oxide thin film deposition and the formation of interfacial 2DEGs. *J. Appl. Phys.* **2017**, *121*, 105302.
(34) Kane, M. J.; Apsley, N.; Anderson, D. A.; Taylor, L. L.; Kerr, T. Parallel conduction in $GaAs/Al_xGa_{1-x}$ As modulation doped heterojunctions. *J. Phys. C: Solid State Phys.* **1985**, *18*, 5629−5636.
(35) Plumb, N. C.; et al. Mixed Dimensionality of Confined Conducting Electrons in the Surface Region of $SrTiO_3$. *Phys. Rev. Lett.* **2014**, *113*, 086801.
(36) Santander-Syro, A. F.; Dai, J.; Rödel, T. C.; Frantzeskakis, E.; Fortuna, F.; Weht, R.; Rozenberg, M. J. Quantum interference effects of out-of-plane confinement on two-dimensional electron systems in oxides. *Phys. Rev. B: Condens. Matter Mater. Phys.* **2020**, *102*, 075101.
(37) Keller, T.; Volkov, S.; Navickas, E.; Kulkarni, S.; Vonk, V.; Fleig, J.; Stierle, A. Nano-scale oxide formation inside electrochemically-formed Pt blisters at a solid electrolyte interface. *Solid State Ionics* **2019**, *330*, 17−23.
(38) Tranvouez, N.; Steyer, P.; Malchère, A.; Boulet, P.; Capon, F.; Bauer, J.-P.; Pierson, J.-F. Effect of Thermal Stresses Formed during Air Annealing of Amorphous Lanthanum Cuprate Thin Films Deposited on Silicon Substrate. *Coatings* **2020**, *10*, 613.
(39) Trier, F.; Christensen, D. V.; Pryds, N. Electron mobility in oxide heterostructures. *J. Phys. D: Appl. Phys.* **2018**, *51*, 293002.
(40) van Delft, M. R.; et al. Sondheimer oscillations as a probe of non-ohmic flow in WP_2 crystals. *Nat. Commun.* **2021**, *12*, 4799.
(41) Singh, G.; Jouan, A.; Hurand, S.; Feuillet-Palma, C.; Kumar, P.; Dogra, A.; Budhani, R.; Lesueur, J.; Bergeal, N. Effect of disorder on

https://doi.org/10.1021/acs.nanolett.1c03198
Nano Lett. 2022, 22, 65−72

superconductivity and Rashba spin-orbit coupling in $LaAlO_3/SrTiO_3$ interfaces. *Phys. Rev. B: Condens. Matter Mater. Phys.* **2017**, *96*, 024509.
(42) Biscaras, J.; Hurand, S.; Feuillet-Palma, C.; Rastogi, A.; Budhani, R. C.; Reyren, N.; Lesne, E.; Lesueur, J.; Bergeal, N. Limit of the electrostatic doping in two-dimensional electron gases of $LaXO_3$(X = Al, Ti)/$SrTiO_3$. *Sci. Rep.* **2015**, *4*, 6788.
(43) Aeschlimann, R.; Preziosi, D.; Scheiderer, P.; Sing, M.; Valencia, S.; Santamaria, J.; Luo, C.; Ryll, H.; Radu, F.; Claessen, R.; Piamonteze, C.; Bibes, M. A Living-Dead Magnetic Layer at the Surface of Ferrimagnetic $DyTiO_3$ Thin Films. *Adv. Mater.* **2018**, *30*, 1707489.
(44) Vicente-Arche, L. M.; Brehin, J.; Varotto, S.; Cosset-Cheneau, M.; Mallik, S.; Salazar, R.; Noel, P.; Vaz, D. C.; Trier, F.; Bhattacharya, S.; Sander, A.; Le Fevre, P.; Bertran, F.; Saiz, G.; Menard, G.; Bergeal, N.; Barthelemy, A.; Li, H.; Lin, C.-C.; Nikonov, D. E.; Young, I. A.; Rault, J.; Vila, L.; Attane, J.-P.; Bibes, M. Spin-charge interconversion in KTaO3 two-dimensional electron gases. *Adv. Mater.* **2021**, 202102102.

https://doi.org/10.1021/acs.nanolett.1c03198
Nano Lett. 2022, 22, 65−72